Key Points:
- Joint inversion of Swarm and CHAMP data from magnetospheric and ocean tidal currents reveals global features of the upper mantle and MTZ
- Integrated imaging of the mantle electrical conductivity from multiple sources significantly improves resolution
- Retrieved conductivity profiles are compatible with a pyrolytic composition and a moderate mantle water content

Joint inversion of satellite-detected tidal and magnetospheric signals constrains electrical conductivity and water content of the upper mantle and transition zone

A. V. Grayver[1] (iD), F. D. Munch[1], A. V. Kuvshinov[1] (iD), A. Khan[1] (iD), T. J. Sabaka[2] (iD), and L. Tøffner-Clausen[3] (iD)

[1]Institute of Geophysics, ETH Zürich, Zürich, Switzerland, [2]Geodesy and Geophysics Laboratory NASA/GSFC, Greenbelt, Maryland, USA, [3]DTU Space, Technical University of Denmark, Copenhagen, Denmark

Abstract We present a new global electrical conductivity model of Earth's mantle. The model was derived by using a novel methodology, which is based on inverting satellite magnetic field measurements from different sources simultaneously. Specifically, we estimated responses of magnetospheric origin and ocean tidal magnetic signals from the most recent Swarm and CHAMP data. The challenging task of properly accounting for the ocean effect in the data was addressed through full three-dimensional solution of Maxwell's equations. We show that simultaneous inversion of magnetospheric and tidal magnetic signals results in a model with much improved resolution. Comparison with laboratory-based conductivity profiles shows that obtained models are compatible with a pyrolytic composition and a water content of 0.01 wt % and 0.1 wt % in the upper mantle and transition zone, respectively.

1. Introduction

Electromagnetic (EM) sounding is an important technique for studying Earth's interior and its material properties. It can be used to infer electrical conductivity in depth and map its lateral variations within the Earth, thereby carrying information about composition, temperature, and presence of water or melt in the mantle [*Karato*, 2011; *Katsura and Yoshino*, 2015; *Khan*, 2016]. Natural EM methods operate in a wide frequency range, corresponding to sounding depths from crust to lower mantle. However, across this wide frequency range several excitation mechanisms coexist [*Kuvshinov*, 2008]. This requires adjustments in the source parametrization during data processing and modeling stages. Therefore, interpretation of these data is usually done separately, resulting in reduced resolution of individual models and potentially causing inconsistencies between them.

Simultaneous inversion of multiple data sets from different sources should lead to improved resolution and smaller uncertainties, and, as a consequence, additional constraints on the fundamental aspects of the composition, structure, and dynamics of the Earth. For instance, *Egbert et al.* [1992] and *Bahr et al.* [1993] estimated responses using ionospheric and magnetospheric signals and obtained regional conductivity models of the upper and lower mantle with better resolutions due to wider frequency range of the combined responses. However, these studies used only land observatory data. Since then, operation of low-orbit satellites (Oersted, CHAMP, SAC-C, and Swarm) [*Olsen et al.*, 2013] has provided a wealth of data opening new opportunities for mantle conductivity studies. In contrast to land observatories, processing of data coming from constantly moving satellites is more challenging, since it requires a careful separation of the magnetic fields from different sources. Recently, new data processing approaches have experienced a significant progress [*Sabaka et al.*, 2015], enabling the usage of both time-varying magnetospheric and tidal magnetic fields for global EM sounding. However, sensitivity of the methods depends on frequency content and mechanism of excitation. For instance, long-period (periods >1.5 days) magnetospheric responses are more sensitive to the conductivity in the mantle transition zone (MTZ) and below [*Kuvshinov and Olsen*, 2006; *Velímský et al.*, 2006; *Civet et al.*, 2015], whereas tidal magnetic signals, specifically signals due to lunar principal semidiurnal M_2 tide, are more sensitive to upper mantle conductivity [*Grayver et al.*, 2016]. As a consequence, simultaneous inversion is expected to provide improved depth resolution. To corroborate this here, we perform inversions

of magnetic data derived from the most recent satellite data and compare individual and joint inversion results, in addition to comparison with laboratory-based conductivity profiles for the purpose of making thermo-chemical inferences.

2. Methods

2.1. Satellite Data

2.1.1. Magnetospheric Responses

For periods longer than 1 day, signals due to magnetospheric ring current dominates the measured time-varying magnetic fields [cf. *Püthe et al.*, 2015a]. These signals are conventionally described by the first zonal spherical harmonic. In this work, we derived magnetospheric responses through the so called $Q_1^0(\omega)$ response [e.g., *Püthe and Kuvshinov*, 2013], which relates frequency-dependent inducing, $\epsilon_1^0(\omega)$, and induced, $\iota_1^0(\omega)$, coefficients as

$$\iota_1^0(\omega) = Q_1^0(\omega)\epsilon_1^0(\omega). \tag{1}$$

From this, the global C_1 response [e.g., *Olsen*, 1999] on the surface of the Earth can be calculated as

$$C_1(\omega) = \frac{a}{2}\frac{1 - 2Q_1^0(\omega)}{1 + Q_1^0(\omega)}. \tag{2}$$

Note that for a radially homogeneous Earth, C_1 responses exhibit monotonic growth with respect to the period $\left(T = \frac{2\pi}{\omega}\right)$.

To quantify the degree of correlation between the inducing and induced coefficients, we used squared coherence given by

$$\mathrm{coh}^2(\omega) = \frac{|\left\langle \iota_1^0(\omega), \epsilon_1^0(\omega)\right\rangle|^2}{\left\langle \iota_1^0(\omega), \iota_1^0(\omega)\right\rangle \left\langle \epsilon_1^0(\omega), \epsilon_1^0(\omega)\right\rangle}, \tag{3}$$

where $\langle\,,\rangle$ stands for inner product between two vectors. In this context, vectors are given by a set of the Fourier-transformed windows of $\iota_1^0(t)$ and $\epsilon_1^0(t)$ time series. The closer this value to its upper bound of one, the more variability in $\iota_1^0(\omega)$ can be explained by the variability in $\epsilon_0^1(\omega)$.

2.1.2. Tidal Magnetic Signals

The tidally induced flow of the electrically conductive ocean water in Earth's main magnetic field generates electric currents, which in turn induce secondary EM field in the subsurface as a result of which the total magnetic field measured on land or at a satellite carries information about the subsurface electrical structure. In contrast to other conventional EM sources of ionospheric and magnetospheric origin, which are inductively coupled with the Earth, the unique characteristic of the motionally induced ocean currents is its galvanic coupling with the Earth. This enhances sensitivity to the resistive subsurface structures since the induced fields are influenced by the toroidal (galvanic) part of the primary tidal EM field.

Despite small amplitude, tidal magnetic signals due to the semidiurnal lunar M_2 tide (period of 12 h and 25 min) have been reliably extracted from satellite measurements using the Comprehensive Inversion approach based on the simultaneous robust least squares estimators of different contributions (core, crust, etc.) and careful preselection of data [*Sabaka et al.*, 2015, 2016]. They were used to retrieve upper mantle conductivity under the oceanic crust [*Grayver et al.*, 2016]. The inverted signals are represented by the radial magnetic field component $B_r^{M_2}$ at the satellite altitude.

2.2. Forward Modeling

In this work, we focus on determining the radial conductivity structure under the oceans and continents. However, to accurately calculate electromagnetic responses due to magnetospheric or tidally induced oceanic currents, it is essential to account for nonuniform oceans [*Everett et al.*, 2003; *Kuvshinov*, 2008]. To this end, we added a heterogeneous conductivity layer corresponding to oceans and continents on top of the laterally homogeneous model (Figure 1). Calculating the EM field for such a 3-D model requires solution of Maxwell's equations

$$\begin{aligned} \mu_0^{-1}\nabla \times \vec{B} &= \sigma\vec{E} + \vec{j}^{\mathrm{ext}}, \\ \nabla \times \vec{E} &= i\omega\vec{B} \end{aligned}, \tag{4}$$
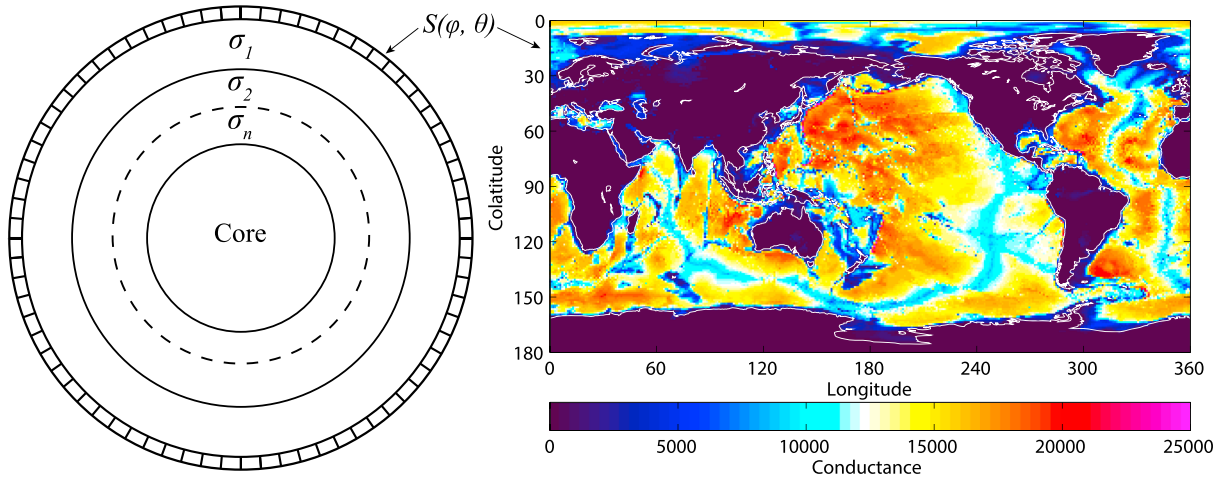
Figure 1. Model parametrization adopted in this study. The model consists of a laterally varying topmost conductivity layer and a number of laterally homogeneous conductivity layers underneath.

where $\vec{E}$ and $\vec{B}$ are electric and magnetic fields, respectively; μ_0 is magnetic permeability of vacuum; σ is electrical conductivity; ω is the angular frequency; and $\vec{j}^{\text{ext}}$ is the extraneous current. We assume $e^{-i\omega t}$ sign convention.

To solve system (4) numerically, we used global solver [*Kuvshinov*, 2008] based on the integral equation approach.

For tidal flow, the extraneous current is confined to the oceans and is given by

$$\vec{j}^{\text{ext}}(\phi, \theta) = \sigma_s(\phi, \theta)\left(\vec{v}(\phi, \theta) \times \vec{B}^{\text{main}}(\phi, \theta)\right), \tag{5}$$

where σ_s is the conductivity of seawater, $\vec{B}^{\text{main}}$ is the Earth's main (core) magnetic field, $\vec{v} = \vec{u}/h$, h is the height of the water column, and $\vec{u}$ is the depth-integrated seawater velocity due to tidal forces. Symbols ϕ and θ denote, respectively, longitude and colatitude. See *Grayver et al.* [2016] for more details about equation (5) individual terms.

For the global $Q_1^0(\omega)$ response, which we need to derive the global C_1 response, the extraneous source current is parameterized using a single $S_1^0(\theta) = \cos\theta$ spherical harmonic. The source is then represented as a current sheet located above the Earth's surface. Once system (4) is solved for the given current distribution, and the radial component of the magnetic field, B_r, at the Earth's surface is obtained, the $Q_1^0(\omega)$ is expressed via surface integral in geomagnetic coordinates as

$$Q_1^0(\omega) = \frac{3}{8\pi}\iint_S\left(B_r(\omega, \vec{r}) - \vec{B}_r^{\text{ext}}(\omega, \vec{r})\right)S_1^0(\theta_{\text{GM}})\text{d}s, \tag{6}$$

where B_r^{ext} is the external magnetic field, $\vec{r} = (r = a, \phi_{\text{GM}}, \theta_{\text{GM}})$ is the position vector in geomagnetic coordinates on the surface of the Earth, and $a = 6371.2$ km is the mean radius of the Earth.

2.3. Stochastic Inversion of Multisource Data

The unknown conductivity values $\sigma_1 \cdots \sigma_N$ (Figure 1) can be estimated from satellite responses by solving a nonlinear inverse problem, which we formulate as a minimization task

$$\underset{\mathbf{m}}{\text{argmin}}\left(\frac{\phi_d(\mathbf{m})}{2} + \frac{\beta}{p_m}\sum_{i=1}^{M}|\mathbf{l}_i\mathbf{m}|^{p_m}\right), \tag{7}$$

where $\mathbf{m} = [\lambda(\sigma_1)\cdots\lambda(\sigma_M)] \in \mathbb{R}^M$ is the vector of unknown model parameters and $\lambda(\cdot)$ represents a log-based transformation ensuring positivity of the argument [e.g., *Key*, 2016]; β is a regularization parameter; $\mathbf{l}_i$ is a regularization operator for the ith model parameter; and scalar p_m controls the norm of the regularization term.
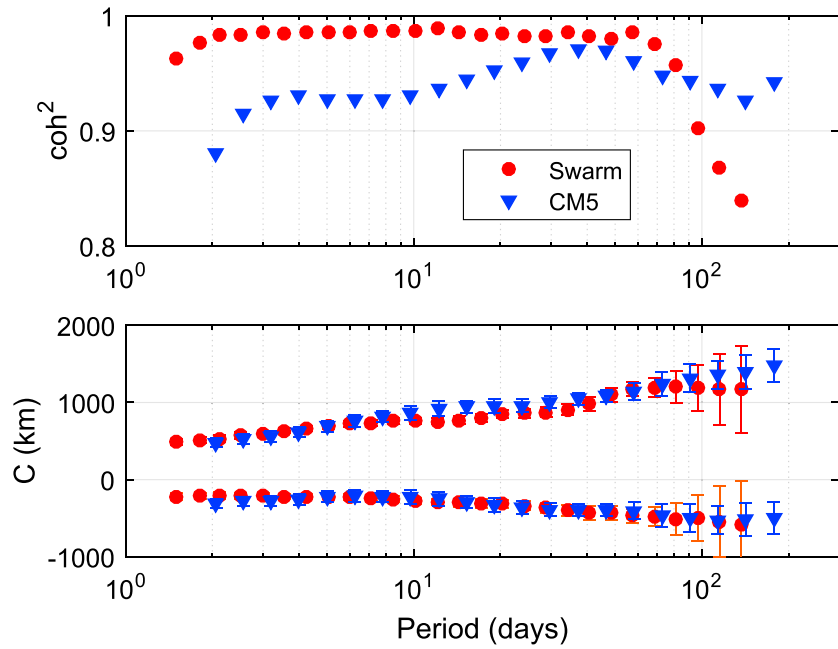
Figure 2. C_1 responses and their squared coherences estimated from Swarm (November 2013 to December 2016) and CM5 data (CHAMP, Oersted, and SAC-C). Positive and negative values represent real and imaginary parts of the response, respectively.

By varying p_m, one retrieves different regularization norms, ranging from smooth L_2-norm ($p_m = 2$) to structurally sparse L_1-norm ($p_m = 1$) solutions. Special attention is paid to the data misfit term given by

$$\phi_d(\mathbf{m}) = \sum_{k \in \mathcal{M}} \left(\frac{1}{N_k} \sum_{i=1}^{N_k} \left| w_i^k \left(f_i^k(\mathbf{m}) - d_i^k \right) \right|^2 \right), \qquad (8)$$

where $\mathcal{M}$ is a set of methods and $\mathbf{w}^k$, $\mathbf{f}^k(\mathbf{m})$, and $\mathbf{d}^k$ are corresponding data weights (reciprocal of uncertainties), forward operator, and observed data, respectively. Note that normalizing with the number of actual measurements (N_k) is an important aspect that helps balance contributions of different methods in the total misfit term of the minimized functional. In general, the approach can be extended to any number of methods but here is limited to methods discussed in section 2.1.

Finally, the minimization problem (7) is solved by using a stochastic optimization algorithm as described in *Grayver and Kuvshinov* [2016].

3. Results

3.1. Satellite Data

To estimate global C_1 responses, we used satellite magnetic measurements. The responses were derived from 37 months (from December 2013 to January 2017) of Swarm data for periods of 1.5–87 days (Figure 2). For periods >90 days, we took responses derived from the much longer CM5 (combined CHAMP, Oersted, and SAC-C data) time series [*Sabaka et al.*, 2015]. In order to better account for the complexity of the source, the magnetospheric time series were parametrized using spherical harmonics up to degree $n = 2$ and order $m = 1$, although only the term corresponding to the $n = 1$, $m = 0$ was used to estimate C_1 responses in the frequency domain. This choice is justified since this term is dominant [e.g., *Shore et al.*, 2016] and most sensitive to the radial structure of the Earth [*Kuvshinov*, 2008], which we aim to recover in this study. Figure 2 shows statistically estimated responses, their uncertainties and squared coherencies. Clearly, using Swarm data results in higher coherency for periods up to ≈90 days. For longer periods, coherency drops because of still insufficient length of the Swarm time series. In contrast, responses estimated from the CM5 data exhibit lower coherencies for periods <90 days, but due to longer time series (≈12 years), longer periods up to 177 days are better resolved. This motivated our decision to combine responses from different missions. Additionally, we used magnetic signals due to the semidiurnal M_2 lunar tide extracted from 12 years of satellite data [*Sabaka et al.*, 2015]. The radial magnetic field component (Figure 3) of this signal was used in the inversion.
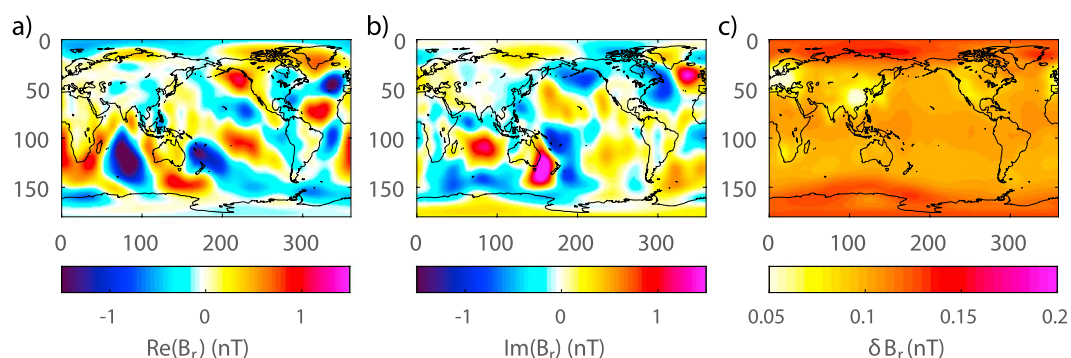
Figure 3. (a) Real and (b) imaginary parts of the radial magnetic field component due to semidiurnal M_2 tide at 430 km altitude. (c) Standard deviation of the signals; note the different scale.

3.2. Inversion

In this study, the subsurface was parametrized using 45 layers ranging in thickness from 9 km right under the oceans and continents to 120 km at the core-mantle boundary where a metal conductor ($\sigma = 10^5$ S/m) is assumed. The starting model was a homogeneous spherical shell of 0.2 S/m.

Figure 4 shows models obtained by inverting satellite magnetospheric and ocean tidal signals separately and jointly. Notably, inversion of C_1 responses fails to 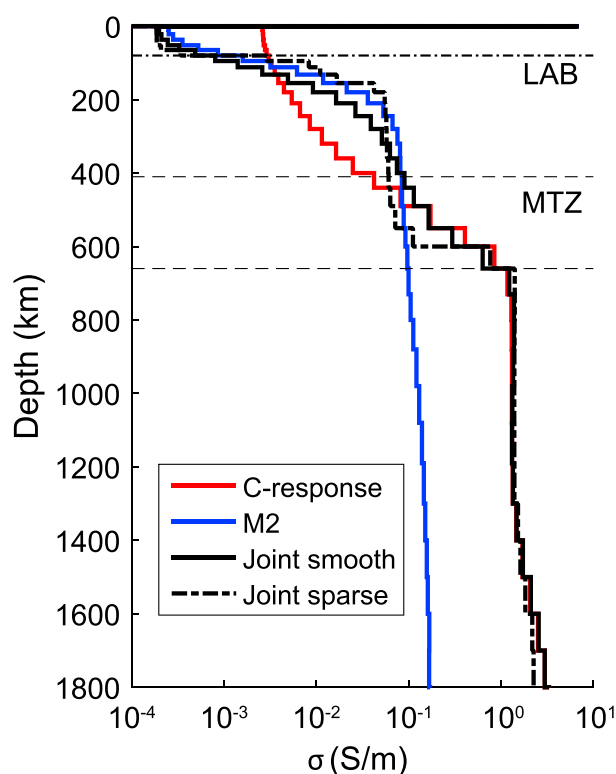recover a prominent boundary between the lithosphere and asthenosphere, which results from the lack of resolution in the upper mantle [*Püthe et al.*, 2015b]. This is not surprising given that the shortest period for C_1 responses is 1.5 days (Figure 2). In contrast, the conductivity model obtained by inverting tidal magnetic signals displays a sharp conductivity increase around the lithosphere-asthenosphere boundary (LAB) at the depth of 70–80 km but does not show any large variations below $\approx$300 km, where it attains a value close to the initial conductivity model. The models obtained from the joint inversion of magnetospheric C_1 responses and tidal magnetic signals managed to resolve the LAB and at the same time constrain conductivity of the mantle transition zone (MTZ) and below. We used different types of regularization norms to produce smooth and structurally sparse models. Both models fit data virtually equally well, attesting to the nonuniqueness of the inverse problem and data uncertainties.

Figure 4. Global conductivity models derived from separate and joint inversions of satellite data. The C-response profile denotes the model obtained by inverting magnetospheric ring current responses, and the $M2$ model denotes the global profile derived from the magnetic tidal signals due to semidiurnal M_2 tide. Joint inversions were performed using smoothing and structurally sparse (L_1-norm) regularization. Individual models were calculated with smoothing regularization. For reference, values for the average lithosphere-asthenosphere boundary under the oceans and mantle transition zone are plotted as dashed horizontal lines.

Let us now examine the data responses these models produce. Figure 5a shows observed C_1 responses as well as responses calculated using the models from Figure 4. One sees that the responses calculated for the models derived from the inversion of C_1 responses alone and the joint inversion model fit data within uncertainties, whereas the M_2 model produces substantially different responses. While the real part of C_1 responses for the M_2 model is close to the observed data for periods <10 days, the imaginary part differs for
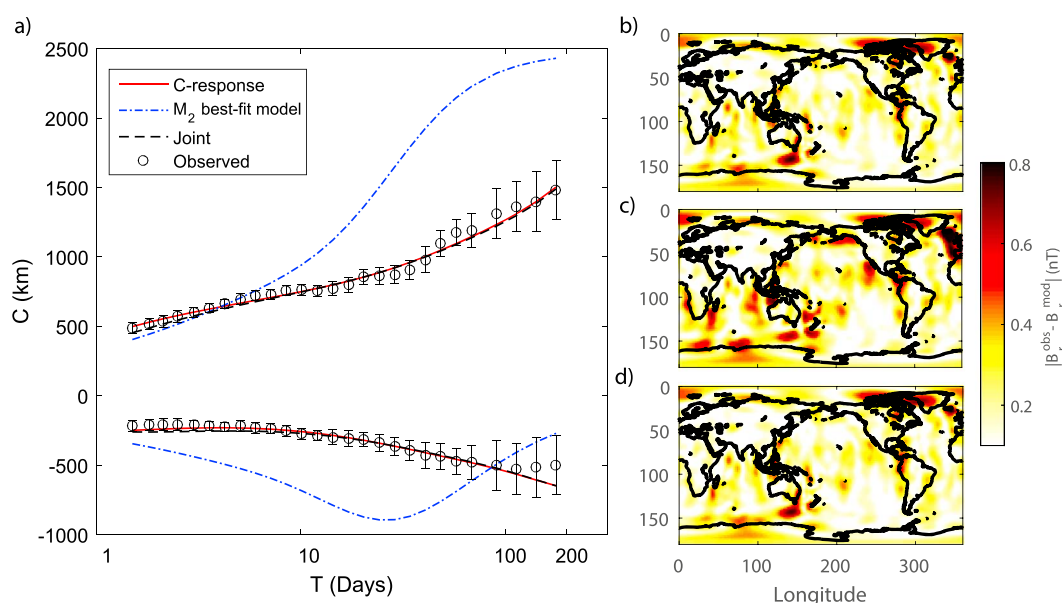
Figure 5. (a) Observed and calculated global C_1 responses for models shown in Figure 4. Positive and negative values represent real and imaginary parts of the response, respectively. (b–d) Magnitude of the radial magnetic field component residuals between observed tidal signals and their predicted counterparts for the models shown in Figure 4: models obtained by inverting tidal magnetic signals only (Figure 5b), magnetospheric C_1 responses only (Figure 5c), and both simultaneously (Figure 5d).

all periods. This behavior is confirmed through synthetic tests (see supporting information) and is to be expected since the M_2 model is not forced to fit C_1 responses. Further, Figures 5b–5d show absolute residuals between observed and predicted tidal magnetic signals. Here we see that the residuals are systematically larger for the C_1-response model (Figure 5c), with differences reaching up 40% of the original signal amplitude. For instance, the residuals are large in regions around South Africa, west of Australia, around New Zealand, west of California, and south of Alaska. This suggests that the increase in conductivity at the LAB that is missing in this model is required to explain the data. Indeed, and as expected, both the M_2 and joint inversion models explain tidal magnetic signals equally well (cf. Figure 5b and 5d). Note that since joint smooth and sparse (L_1-norm) models produce virtually identical responses, only smooth model responses are shown in Figure 5.

3.3. Comparison With Laboratory-Based Conductivity Profiles

Joint inversion models seem to constrain upper and midmantle conductivities better than individual inversions. Therefore, it is instructive to interpret these models. To this end, we compute laboratory-based bulk electrical conductivity profiles using the approach of *Khan* [2016]. Bulk electrical conductivity is estimated from the mineralogy and databases of laboratory mineral conductivity measurements. The equilibrium rock mineralogy, including elastic moduli and density, is computed by free-energy minimization [*Connolly*, 2009] as a function of pressure, temperature, and bulk composition using the thermodynamic formulation and data compiled by *Stixrude and Lithgow-Bertelloni* [2011]. We model mantle composition using the Na_2O-CaO-FeO-MgO-Al_2O_3-SiO_2 chemical system; bulk rock conductivity and elastic properties are estimated by employing appropriate averaging techniques. The pressure profile is obtained by integrating the load from the surface. We compute bulk electrical conductivity profiles for a pyrolytic mantle and a standard temperature of 1390°C at the base of an 80 km thick lithosphere [*Katsura et al.*, 2010]. The sublithospheric mantle adiabat is defined by the entropy of the lithology at the base of the lithosphere, whereas in the lithosphere, temperature is computed by a linear geothermal gradient (see supporting information). Elastic properties and density produced by this thermo-chemical model agree remarkably well with preliminary reference Earth model (see supporting information) of *Dziewonski and Anderson* [1981].

Figure 6 shows a number of laboratory-based conductivity profiles calculated for different mantle mineral water contents and plotted together with the joint inversion results. For present purposes, we varied the water content of olivine, garnet, and wadsleyite. The water contents of clinopyroxene, orthopyroxene, and ringwoodite are estimated using the water partition coefficients described in *Khan* [2016], which are based on
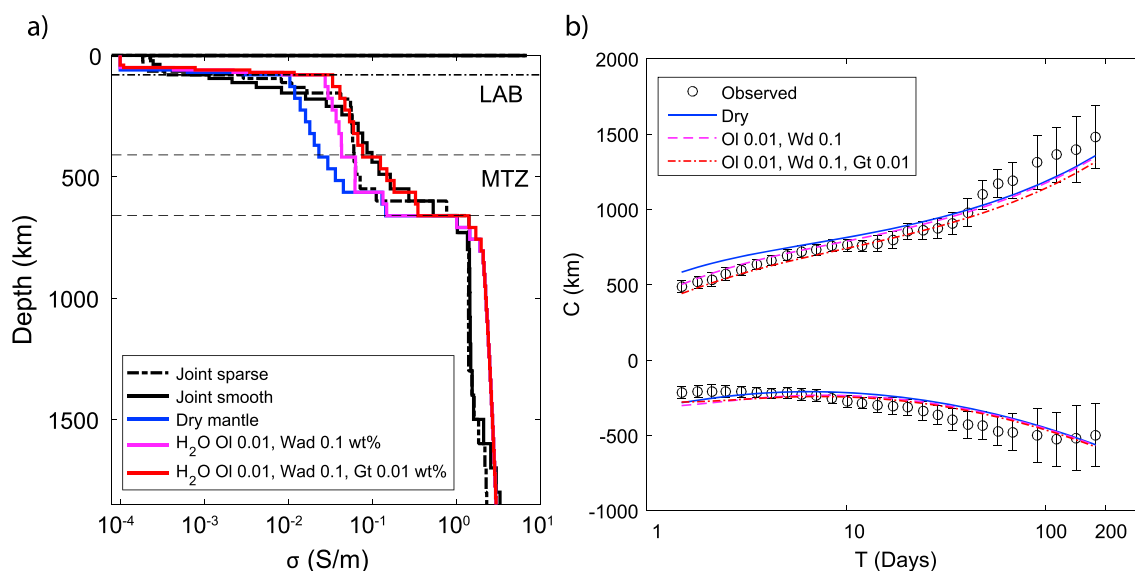
Figure 6. (a) Comparison of conductivity models obtained from inversion of satellite data and several laboratory-based conductivity profiles calculated following the approach of *Khan* [2016]. The laboratory-based profiles are based on the assumption of a pyrolytic mantle and different water contents in olivine (Ol), wadsleyite (Wad), and garnet (Gr). (b) Global C_1 responses calculated for the laboratory-based conductivity profiles shown in Figure 6a. Observed responses are shown with circles. Positive and negative values represent real and imaginary parts of the response, respectively.

the measurements of *Inoue et al.* [2010] and *Férot and Bolfan-Casanova* [2012]. As is evident from the figure, a dry mantle produces conductivities which are much lower than the conductivity of the models obtained from the joint inversion. Moderate amounts of water [*Karato*, 2011; *Khan and Shankland*, 2012], 0.01 wt % in olivine and 0.1 wt % in wadsleyite, in the upper mantle and transition zone result in conductivities which are much closer to the inverted models. An increase of 0.01 wt % in the water content of garnet results in higher conductivities throughout the upper mantle and MTZ improving the match to the smooth model and observations (Figure 6b). However, these differences are likely within the uncertainty of our models and should be considered with caution. The conductivity of the lower mantle in the inverted models is close to the laboratory predictions.

While this interpretation is qualitative and a direct inversion in terms of thermo-chemical parameters is more appropriate [*Khan*, 2016], these results stress that conductivity models obtained from joint inversion of data from very different sources produce self-consistent models. The thermo-chemical modeling combined with laboratory measurements of the electrical conductivity further confirms that these models are consistent with plausible mantle properties and moderate water contents, in addition to radial seismic reference models (see supporting information).

4. Conclusions

The inversion of natural source EM data for Earth's mantle electrical conductivity usually relies on single-source data and therefore faces the problem of limited resolution at different depths due to limits in frequency range imposed by varying source morphology. We showed that inverting data from magnetospheric and ocean tidal sources simultaneously yields a consistent conductivity profile of the upper mantle and transition zone. The obtained global profile is capable of fitting individual data types as well as separate inversions and efficiently exploits sensitivity overlap between different sources.

The new conductivity profile provides additional constraints on estimations of geophysically relevant mantle properties through comparisons with laboratory-based conductivity profiles. Specifically, assuming a pyrolytic mantle composition and the temperature of $T = 1380°C$ at LAB, we found that a moderate amount of water is necessary to explain the observed conductivity values in the asthenosphere and MTZ. However, for the upper mantle, this profile is more representative of the mantle under the oceans since tidal signals are negligible above continents. Taking these points into account, the new model can serve as a new reference

for studies, which need to account for mantle conductivity such as in space weather or oceanography. Finally, the approach of jointly inverting multisource data can significantly help studies that aim at mapping lateral variations in mantle conductivity.

References

Bahr, K., N. Olsen, and T. J. Shankland (1993), On the combination of the magnetotelluric and the geomagnetic depthsounding method for resolving an electrical conductivity increase at 400 km depth, *Geophys. Res. Lett.*, *20*(24), 2937–2940.

Civet, F., E. Thébault, O. Verhoeven, B. Langlais, and D. Saturnino (2015), Electrical conductivity of the Earth's mantle from the first Swarm magnetic field measurements, *Geophys. Res. Lett.*, *42*, 3338–3346, doi:10.1002/2015GL063397.

Connolly, J. (2009), The geodynamic equation of state: What and how, *Geochem. Geophys. Geosyst.*, *10*, Q10014, doi:10.1029/2009GC002540.

Dziewonski, A. M., and D. L. Anderson (1981), Preliminary reference Earth model, *Phys. Earth Planet. Inter.*, *25*(4), 297–356.

Egbert, G. D., J. R. Booker, and A. Schultz (1992), Very long period magnetotellurics at Tucson Observatory: Estimation of impedances, *J. Geophys. Res.*, *97*(B11), 15,113–15,128.

Everett, M. E., S. Constable, and C. G. Constable (2003), Effects of near-surface conductance on global satellite induction responses, *Geophys. J. Int.*, *153*(1), 277–286.

Férot, A., and N. Bolfan-Casanova (2012), Water storage capacity in olivine and pyroxene to 14 GPa: Implications for the water content of the Earth's upper mantle and nature of seismic discontinuities, *Earth Planet. Sci. Lett.*, *349*, 218–230.

Grayver, A. V., and A. V. Kuvshinov (2016), Exploring equivalence domain in non-linear inverse problems using covariance matrix adaption evolution strategy (CMAES) and random sampling, *Geophys. J. Int.*, *205*, 971–987, doi:10.1093/gji/ggw063.

Grayver, A. V., N. R. Schnepf, A. V. Kuvshinov, T. J. Sabaka, C. Manoj, and N. Olsen (2016), Satellite tidal magnetic signals constrain oceanic lithosphere-asthenosphere boundary, *Sci. Adv.*, *2*(9), e1600798.

Inoue, T., T. Wada, R. Sasaki, and H. Yurimoto (2010), Water partitioning in the Earth's mantle, *Phys. Earth Planet. Inter.*, *183*(1), 245–251.

Karato, S.-I. (2011), Water distribution across the mantle transition zone and its implications for global material circulation, *Earth Planet. Sci. Lett.*, *301*(3), 413–423.

Katsura, T., and T. Yoshino (2015), Heterogeneity of electrical conductivity in the oceanic upper mantle, in *The Earth's Heterogeneous Mantle*, edited by A. Khan and F. Deschamps, pp. 173–204, Springer Int., New York, doi:10.1007/978-3-319-15627-9_6.

Katsura, T., A. Yoneda, D. Yamazaki, T. Yoshino, and E. Ito (2010), Adiabatic temperature profile in the mantle, *Phys. Earth Planet. Inter.*, *183*(1), 212–218.

Key, K. (2016), MARE2DEM: a 2-D inversion code for controlled-source electromagnetic and magnetotelluric data, *Geophys. J. Int.*, *207*(1), 571–588.

Khan, A. (2016), On earth's mantle constitution and structure from joint analysis of geophysical and laboratory-based data: An example, *Surv. Geophys.*, *37*(1), 149–189, doi:10.1007/s10712-015-9353-z.

Khan, A., and T. Shankland (2012), A geophysical perspective on mantle water content and melting: Inverting electromagnetic sounding data using laboratory-based electrical conductivity profiles, *Earth Planet. Sci. Lett.*, *317*, 27–43.

Kuvshinov, A. (2008), 3-D global induction in the oceans and solid Earth: Recent progress in modeling magnetic and electric fields from sources of magnetospheric, ionospheric and oceanic origin, *Surv. Geophys.*, *29*(2), 139–186.

Kuvshinov, A., and N. Olsen (2006), A global model of mantle conductivity derived from 5 years of CHAMP, Ørsted, and SAC-C magnetic data, *Geophys. Res. Lett.*, *33*, L18301, doi:10.1029/2006GL027083.

Olsen, N. (1999), Long-period (30 days–1 year) electromagnetic sounding and the electrical conductivity of the lower mantle beneath Europe, *Geophys. J. Int.*, *138*(1), 179–187.

Olsen, N., et al. (2013), The Swarm Satellite Constellation Application and Research Facility (SCARF) and Swarm data products, *Earth Planets Space*, *65*(11), 1189–1200.

Püthe, C., and A. Kuvshinov (2013), Determination of the 1-D distribution of electrical conductivity in Earth's mantle from Swarm satellite data, *Earth Planets Space*, *65*(11), 1233–1237.

Püthe, C., A. Kuvshinov, and N. Olsen (2015a), Handling complex source structures in global EM induction studies: From C-responses to new arrays of transfer functions, *Geophys. J. Int.*, *201*(1), 318–328.

Püthe, C., A. Kuvshinov, A. Khan, and N. Olsen (2015b), A new model of Earth's radial conductivity structure derived from over 10 yr of satellite and observatory magnetic data, *Geophys. J. Int.*, *203*(3), 1864–1872.

Sabaka, T. J., N. Olsen, R. H. Tyler, and A. Kuvshinov (2015), CM5, a pre-Swarm comprehensive geomagnetic field model derived from over 12 yr of CHAMP, ørsted, SAC-C and observatory data, *Geophys. J. Int.*, *200*(3), 1596–1626.

Sabaka, T. J., R. H. Tyler, and N. Olsen (2016), Extracting ocean-generated tidal magnetic signals from Swarm data through satellite gradiometry, *Geophys. Res. Lett.*, *43*, 3237–3245, doi:10.1002/2016GL068180.

Shore, R., K. Whaler, S. Macmillan, C. Beggan, J. Velímskỳ, and N. Olsen (2016), Decadal period external magnetic field variations determined via eigenanalysis, *J. Geophys. Res. Space Physics*, *121*, 5172–5184, doi:10.1002/2015JA022066.

Stixrude, L., and C. Lithgow-Bertelloni (2011), Thermodynamics of mantle minerals-II. Phase equilibria, *Geophys. J. Int.*, *184*(3), 1180–1213.

Velímskỳ, J., Z. Martinec, and M. E. Everett (2006), Electrical conductivity in the Earth's mantle inferred from CHAMP satellite measurements—I. Data processing and 1-D inversion, *Geophys. J. Int.*, *166*(2), 529–542.